Published in final edited form as:
Phys Med Biol. 2010 August 21; 55(16): 4625–4645. doi:10.1088/0031-9155/55/16/002.

A parallel adaptive finite element simplified spherical harmonics approximation solver for frequency domain fluorescence molecular imaging

Yujie Lu[1], **Banghe Zhu**[1], **Haiou Shen**[2], **John C Rasmussen**[1], **Ge Wang**[2], and **Eva M Sevick-Muraca**[1]

Yujie Lu: yujie.lu@uth.tmc.edu

[1] Center for Molecular Imaging, The Brown Foundation Institute of Molecular Medicine, University of Texas Health Science Center at Houston, 1825 Pressler Street, Houston, TX 77030, USA

[2] School of Biomedical Engineering and Sciences, Virginia Tech, Blacksburg, VA, USA

Abstract

Fluorescence molecular imaging/tomography may play an important future role in preclinical research and clinical diagnostics. Time- and frequency-domain fluorescence imaging can acquire more measurement information than the continuous wave (CW) counterpart, improving the image quality of fluorescence molecular tomography. Although diffusion approximation (DA) theory has been extensively applied in optical molecular imaging, high-order photon migration models need to be further investigated to match quantitation provided by nuclear imaging. In this paper, a frequency-domain parallel adaptive finite element solver is developed with simplified spherical harmonics (SP_N) approximations. To fully evaluate the performance of the SP_N approximations, a fast time-resolved tetrahedron-based Monte Carlo fluorescence simulator suitable for complex heterogeneous geometries is developed using a convolution strategy to realize the simulation of the fluorescence excitation and emission. The validation results show that high-order SP_N can effectively correct the modeling errors of the diffusion equation, especially when the tissues have high absorption characteristics or when high modulation frequency measurements are used. Furthermore, the parallel adaptive mesh evolution strategy improves the modeling precision and the simulation speed significantly on a realistic digital mouse phantom. This solver is a promising platform for fluorescence molecular tomography using high-order approximations to the radiative transfer equation.

1. Introduction

Imaging of the biological actions of therapeutics *in vivo* is paramount for the advancing field of molecular medicine (Weissleder 1999, Massoud and Gambhir 2003, Herschman 2003, Cherry 2004). Currently, nuclear imaging techniques of positron emission tomography (PET), single photon emission computed tomography (SPECT), or gamma scintigraphy are the clinical 'gold-standards' of molecular imaging. These techniques depend upon the collection of high energy photons that emanate from the relaxation of a radionuclide that is targeted to a specific disease marker in order to generate either a planar image (gamma scintigraphy) or a tomographic image (PET and SPECT). Preclinical small animal studies using these techniques are commonplace in the drug discovery field.

Optical molecular imaging is akin to nuclear imaging in that it also involves the collection of photons, albeit low energy photons that have significant attenuation due to scatter and absorption. In contrast to bioluminescence (Contag and Bachmann 2002, Wang *et al* 2004, Alexandrakis *et al* 2005, Chaudhari *et al* 2005, Cong *et al* 2005, Lv *et al* 2006, Dehghani *et*

al 2006, Kuo *et al* 2007, Lu *et al* 2009a, Klose *et al* 2010) or emerging Cherenkov imaging (Cho *et al* 2009, Robertson *et al* 2009) approaches, fluorescence imaging has the capability for higher photon count rate for both planar and tomographic imaging as the fluorescent gene product or fluorescent exogenous agent can be repeatedly excited by tissue surface illumination (Sevick-Muraca *et al* 2002). Although most gene reporters are excited and emit in the visible regime where limited tissue penetration and autofluorescence can confound signals, new fluorescent gene reporters such as IFP1.4 (Shu *et al* 2009) are excited in the red range (>690 nm) with reduced autofluorescence and greater tissue penetration, opening up interesting possibilities for quantitative tomography for preclinical drug discovery. Exogenous agents with near-infrared (NIR) excitation (>780 nm) have minimal tissue autofluorescence thereby offering the lowest background for fluorescence planar and tomography techniques. Indeed, using indocyanine green (ICG), a dim and poor fluorophore with a low quantum efficiency of 0.016, planar human imaging has been conducted even at microdosages of <100 μg and millisecond data acquisition rates (Sevick-Muraca *et al* 2008, Rasmussen *et al*, 2009) to image structures in shallow tissues as well as tissue at depths up to 4–5 cm (Sevick-Muraca *et al* 2008).

Given the high photon count rates of planar fluorescence imaging for both fluorescent gene products and exogenous agents, tomographic reconstruction for quantification of expression/deposition should be possible given an accurate forward model for propagation of light in tissues. For quantification, the forward model must be suitable for visible and red wavelength-excitable gene products in preclinical studies, as well as NIR excitable exogenous agents in preclinical as well as clinical studies. While significant work has been accomplished using the diffusion approximation to the radiative transport equation (RTE) to model light transport in biological tissues (Gibson *et al* 2005), the high tissue absorption associated with visible and red-excited wavelengths, the small tissue volumes of preclinical models, or the shallow depths of human imaging studies obviate its use. A direct solution of the RTE is an alternative (Lewis and Warren 1984, Klose *et al* 2005, Rasmussen *et al* 2006, Joshi *et al* 2008), but with an expense of solving $N(N+2)$ and $(N+1)^2$-coupled partial differential equations corresponding to discrete ordinates (S_N) and spherical harmonics (P_N) methods, where N depicts the approximation degree. High-order approximations have been recently attempted to obtain sufficient performance for model-based iterative image reconstructions with less memory requirement and time cost compared with direct RTE solvers (Klose and Larsen 2006, Cong *et al* 2007, Yuan *et al* 2009, Chu *et al* 2009). However, in order to realize quantitative tomographic reconstruction in complex heterogeneous geometries, such as a mouse, we need to fully evaluate and validate the performance of those high-order approximations.

In addition, time-dependent measurements, i.e. time- or frequency-domain measurements involving pulsed or modulated illumination of excitation light, have been shown to improve reconstructions of embedded fluorescent tissues by providing more information than continuous wave or time-independent methods (Godavarty *et al* 2003), but few, if any, studies validate higher order approximation model predictions of both excitation and fluorescence measurements in both time and 3D space. Owing to the complex and curvilinear geometries associated with biological tissues, finite element methods (FEM) become necessary for accurate quantification especially in small volumes where gradients of excitation and emission fluence distribution contribute substantially to discretization errors. The adaptive finite element method uses local mesh evolution strategy not only to accelerate the simulation with fewer discretized points but also to improve upon the discretization errors, forward solution accuracy and therefore reconstruction quality (Joshi *et al* 2004, Lv *et al* 2006). When the simulation region is decomposed into several subdomains, parallel simulation implementation can effectively accelerate the adaptive FEM simulation (Gu *et al* 2009, Lu and Chatziioannou 2009), enabling fully parallel adaptive finite element photon migration simulation with high-

order RTE approximations that are suitable for use within inverse image reconstruction algorithms (Lu *et al* 2009b).

Herein, the forward solution for frequency domain, fluorescent photon migration in biological tissues, is realized with fully parallel adaptive finite element methods. The simplified spherical harmonics (SP_N) approximations are validated using a unique time-domain tetrahedron-based Monte Carlo (MC) fluorescence simulator utilizing the convolution method (Swartling *et al* 2003) for improvement in computational time. Compared with diffusion approximation, computational validation shows the preferable performance of the SP_N approximations especially in cases of high absorption and high modulation frequency. Simulation performance is then evaluated using a whole-body digital mouse to document improvement arising from parallel adaptive finite element strategies for fluorescence molecular imaging.

In the following section, the proposed simulation framework that incorporates parallel adaptive strategy and SP_N approximations for frequency-domain fluorescence molecular imaging is introduced. The validation and comparative simulation results of the SP_N approximations and MC methods are demonstrated in section 3. The performance and simulation improvements from parallel adaptive mesh evolution are represented in section 4. The conclusion and relevant discussions are provided in section 5. The forward simulation model presented herein represents a platform pertinent to time-dependent and -independent measurements, excitation and emission measurements, as well as emission measurements employing bioluminescence and Cherenkov emission tomography in small animals for drug discovery purposes.

2. Methods

2.1. The simplified spherical harmonics (SP_N) approximations for frequency domain fluorescence molecular imaging

The frequency domain RTE for fluorescence molecular imaging in 3D are (Rasmussen *et al* 2006)

$$\begin{cases} \widehat{\mathbf{s}}\cdot\nabla\psi^{x}(\mathbf{r},\widehat{\mathbf{s}},\omega)+\left(\mu_t^{x}(\mathbf{r})+\frac{i\omega}{c_b(\mathbf{r})}\right)\psi^{x}(\mathbf{r},\widehat{\mathbf{s}},\omega)=\mu_s^{x}(\mathbf{r})\int_{4\pi}p(\widehat{\mathbf{s}},\widehat{\mathbf{s}}')\psi^{x}(\mathbf{r},\widehat{\mathbf{s}}',\omega)\mathrm{d}\widehat{\mathbf{s}} \\ \widehat{\mathbf{s}}\cdot\nabla\psi^{m}(\mathbf{r},\widehat{\mathbf{s}},\omega)+\left(\mu_t^{m}(\mathbf{r})+\frac{i\omega}{c_b(\mathbf{r})}\right)\psi^{m}(\mathbf{r},\widehat{\mathbf{s}},\omega)=\mu_s^{m}(\mathbf{r})\int_{4\pi}p(\widehat{\mathbf{s}},\widehat{\mathbf{s}}')\psi^{m}(\mathbf{r},\widehat{\mathbf{s}}',\omega)\mathrm{d}\widehat{\mathbf{s}}'+\frac{Q\mu_a^{xf}}{1+i\omega\tau}\psi^{x} \end{cases} \quad (1a)\ (1b)$$

where the modulation frequency is ω; $\psi^{x,m}$ are the excitation and emission radiances; $c_b(\mathbf{r})$ is the light speed in the domain Ω; $\mu_t^{x,m}=\mu_s^{x,m}+\mu_a^{x,m}$, $\mu_s^{x,m}$ and $\mu_a^{x,m}$ are the scattering and absorption coefficients, respectively; μ_a^{xf} is the absorption coefficient of the fluorophore; Q and τ are the quantum efficiency and lifetime of the fluorophore, respectively; $p(\hat{\mathbf{s}}, \hat{\mathbf{s}}')$ is the scattering phase function giving the probability of a photon anisotropically scattering from the direction $\hat{\mathbf{s}}'$ to direction $\hat{\mathbf{s}}$. Generally, the Henyey–Greenstein (HG) phase function is often used to characterize this probability (Ishimaru 1997):

$$p(\cos\theta)=\frac{1-g^2}{4\pi(1+g^2-2g\cos\theta)^{3/2}}, \quad (2)$$

where g is the anisotropy parameter; cos θ denotes the scattering angle that is equal to $\hat{\mathbf{s}}\cdot\hat{\mathbf{s}}'$. The HG phase function is easily expanded by the Legendre polynomial and is therefore convenient for numerical computation. The angle-independent fluence $\varphi^{x,m}$ is further defined as

$$\varphi^{x,m}=\int_{4\pi}\psi^{x,m}\mathrm{d}\Omega. \tag{3}$$

At the tissue surface, $r \in \partial\Omega$, we assume that some photons are internally reflected and do not escape from the domain because of the mismatch between the refractive indices n_b of the domain Ω and n_m of the surrounding external medium. Therefore, the partially reflecting boundary condition for $\psi^{x,m}$ is described by (Klose and Larsen 2006)

$$\begin{cases} \psi^{x}(\mathbf{r},\hat{\mathbf{s}},\omega)=S(\mathbf{r},\hat{\mathbf{s}},\omega)+R(\hat{\mathbf{s}}'\cdot\mathbf{v})\psi^{x}(\mathbf{r},\hat{\mathbf{s}}',\omega) & \text{(4a)} \\ \psi^{m}(\mathbf{r},\hat{\mathbf{s}},\omega)=R(\hat{\mathbf{s}}'\cdot\mathbf{v})\psi^{m}(\mathbf{r},\hat{\mathbf{s}}',\omega), & \text{(4b)} \end{cases}$$

where $\mathbf{v}$ is the unit outer normal vector; the incidence angle θ_b from the volume is not beyond the critical angle θ_c ($\theta_c = \arcsin(n_m/n_b)$ based on Snell's law), and where the reflectivity $R(\cos\theta_b)$ is given by (Haskell *et al* 1994)

$$R(\cos\theta_b)=\frac{1}{2}\left[\frac{\sin^2(\theta_b-\theta_m)}{\sin^2(\theta_b+\theta_m)}+\frac{\tan^2(\theta_b-\theta_m)}{\tan^2(\theta_b+\theta_m)}\right], \tag{5}$$

where θ_m is the transmission angle. The exiting partial current $J^{+}(\mathbf{r})$ at each point $\mathbf{r}$ on the volume surface (where the illumination $S(\mathbf{r}, \hat{\mathbf{s}}, \omega)$ is not considered) is given as (Klose and Larsen 2006)

$$J^{+}_{x,m}(\mathbf{r},\omega)=\int_{\hat{\mathbf{s}}\cdot\mathbf{v}>0}[1-R(\hat{\mathbf{s}}\cdot\mathbf{v})](\hat{\mathbf{s}}\cdot\mathbf{v})\psi^{x,m}(\mathbf{r},\hat{\mathbf{s}},\omega)\mathrm{d}\hat{\mathbf{s}}. \tag{6}$$

After a series of deductions with the P_N method, the excitation SP_N approximations are obtained similar to that described by Klose and Larsen (2006)

$$-\left(\frac{n+1}{2n+1}\right)\nabla\cdot\frac{1}{\mu^{x}_{a,n+1}}\nabla\left(\left(\frac{n+2}{2n+3}\right)\gamma^{x}_{n+2}+\left(\frac{n+1}{2n+3}\right)\gamma^{x}_{n}\right)-\left(\frac{1}{2n+1}\right)\nabla\cdot\frac{1}{\mu^{x}_{a,n-1}}\nabla\left(\left(\frac{n}{2n-1}\right)\gamma^{x}_{n}+\left(\frac{n-1}{2n-1}\right)\gamma^{x}_{n-2}\right)+\mu^{x}_{a,n}\gamma^{x}_{n}=0, \tag{7}$$

where $\mu^{x}_{a,n}=\mu^{x}_{a}+\mu^{x}_{s}(1-g^{n})+\iota\omega/c_b$ (Chu *et al* 2009); when ψ^{x} is expanded by the P_N approximation, γ^{x}_{n} are the *Legendre moments* of ψ^{x} ($2 \le n \le N$, N is an odd positive integer). The $(N + 1)/2$ boundary conditions for equation (7) can be obtained (Klose and Larsen 2006). When we define ϕ^{x}_{n} as the *composite moments* of γ^{x}_{n},

$$\begin{gathered} \phi^{x}_{1}=\gamma^{x}_{0}+2\gamma^{x}_{2}, \\ \phi^{x}_{2}=3\gamma^{x}_{2}+4\gamma^{x}_{4}, \\ \cdots, \\ \phi^{x}_{n}=(2n-1)\gamma^{x}_{2n-2}+(2n)\gamma^{x}_{2n}, \\ \cdots, \\ \phi^{x}_{(N+1)/2}=N\gamma^{x}_{N-1}; \end{gathered} \tag{8}$$

the general equations of the SP_N approximations and its boundary conditions for excitation wavelength can be subsequently written as

$$\begin{cases} -\nabla \cdot C^x_{i,\nabla\phi_i} \nabla \phi^x_i + \sum_{j=1}^{(N+1)/2} C^x_{i,\phi_j} \phi^x_j = 0 \\ \sum_{j=1}^{(N+1)/2} C^{b,x}_{i,\nabla\phi_j} \mathbf{v} \cdot \phi^x_j = \sum_{j=1}^{(N+1)/2} C^{b,x}_{i,\phi_j} \phi^x_j + C^x_{i,S} S_i \;\; i \in [1,(N+1)/2], \end{cases} \quad (9a)\ (9b)$$

where $C^x_{i,\nabla\phi_i}, C^x_{i,\phi_j}, C^{b,x}_{i,\nabla\phi_j}, C^{b,x}_{i,\nabla\phi_j}$ and $C^x_{i,S}$ can be calculated for SP_1 to SP_7 (Klose and Larsen 2006). The corresponding approximation and boundary conditions for emission wavelength can be similarly defined as

$$\begin{cases} -\nabla \cdot C^m_{i,\nabla\phi_i} \nabla \phi^m_i + \sum_{j=1}^{(N+1)/2} C^m_{i,\phi_j} \phi^m_j = \frac{Q\mu^{xf}_a}{1+i\omega\tau} \phi^x_i \\ \sum_{j=1}^{(N+1)/2} C^{b,m}_{i,\nabla\phi_j} \mathbf{v} \cdot \phi^m_j = \sum_{j=1}^{(N+1)/2} C^{b,m}_{i,\phi_j} \phi^m_j \;\; i \in [1,(N+1)/2]. \end{cases} \quad (10a)\ (10b)$$

2.2. The parallel adaptive finite element methods for the SP_N approximations

For the finite element analysis, a general weak formulation for the SP_N approximations can be written as (Rao 1999)

$$\begin{cases} \int_\Omega \left\{ C^x_{i,\nabla\phi_i} \nabla \phi^x_i \cdot \nabla \upsilon + \sum_{j=1}^{(N+1)/2} C^x_{i,\phi_j} \phi^x_j \cdot \upsilon \right\} \mathrm{d}\Omega - \int_{\partial\Omega} C^x_{i,\nabla\phi_i} \sum_{j=1}^{(N+1)/2} f_{\mathbf{v}\cdot\phi^x_i}(\phi^x_j) \cdot \upsilon \,\mathrm{d}\,\partial\Omega = \int_{\partial\Omega} C^x_{i,\nabla\phi_i} f_{S_i}(S_i) \cdot \upsilon \,\mathrm{d}\,\partial\Omega \\ \int_\Omega \left\{ C^m_{i,\nabla\phi_i} \nabla \phi^m_i \cdot \nabla \upsilon + \sum_{j=1}^{(N+1)/2} C^m_{i,\phi_j} \phi^m_j \cdot \upsilon \right\} \mathrm{d}\Omega - \int_{\partial\Omega} C^m_{i,\nabla\phi_i} \sum_{j=1}^{(N+1)/2} f_{\mathbf{v}\cdot\phi^m_i}(\phi^m_j) \cdot \upsilon \,\mathrm{d}\,\partial\Omega = \int_\Omega \frac{Q\mu^{xf}_a}{1+i\omega\tau} \phi^x_i \Omega. \end{cases} \quad (11a)\ (11b)$$

To avoid the processing of $\mathbf{v} \cdot \phi^{x,m}_i$ in boundary integration, we assume that $\mathbf{v} \cdot \phi^{x,m}_i$ are unknown variables in the boundary equations ((9b) and (10b)). We obtain $f^{x,m}_{\mathbf{v}\cdot\phi_i}(\cdot)$ and $f_{S_i}(\cdot)$by solving a set of first-order equations to obtain the boundary conditions.

After the simulation domain Ω is discretized into the volumetric mesh $\mathcal{T}$, the mesh is next partitioned into N_c mesh subdomains $\mathcal{T}_c$ ($1 \le \mathcal{T}_c \le N_c$), where N_c is the number of the utilized CPUs. For the finite element implementation, the space of linear finite elements $\mathcal{V}$ is introduced on $\mathcal{T}$. $\phi^{x,m}_i$ are approximated as

$$\phi^{l,x,m}_i(\mathbf{r},\omega) \approx \sum_{p=1}^{N_\mathcal{P}} \phi^{l,x,m}_{i,p}(\omega) \upsilon^l_p(\mathbf{r}), \quad (12)$$

where $\phi^{l,x,m}_{i,p}(\omega)$ are the discretized values at a discretized point p at the lth adaptive mesh for excitation and emission wavelengths when using the basis function $\upsilon_p(\mathbf{r})$; $N_\mathcal{P}$ is the total number of the discretized points over the whole domain. Upon combining equations (11a),(11b), and (12), one obtains

$$\sum_{e=1}^{N_{\mathcal{T}_c}}\begin{bmatrix} m_{1\phi_1}^{l,x,m} & m_{1\phi_2}^{l,x,m} & \cdots & m_{1\phi_{(N+1)/2}}^{l,x,m} \\ m_{2\phi_1}^{l,x,m} & m_{2\phi_2}^{l,x,m} & \cdots & m_{1\phi_{(N+1)/2}}^{l,x,m} \\ \vdots & \vdots & \vdots & \vdots \\ m_{(N+1)/2\phi_1}^{l,x,m} & m_{(N+1)/2\phi_2}^{l,x,m} & \cdots & m_{(N+1)/2\phi_{(N+1)/2}}^{l,x,m} \end{bmatrix}\begin{bmatrix} \phi_{1,\tau_e}^{l,x,m} \\ \phi_{2,\tau_e}^{l,x,m} \\ \vdots \\ \phi_{(N+1)/2,\tau_e}^{l,x,m} \end{bmatrix}=\sum_{e=1}^{N_{\mathcal{T}_c}}\begin{bmatrix} b_{1,\tau_e}^{l,x,m} \\ b_{2,\tau_e}^{l,x,m} \\ \vdots \\ b_{(N+1)/2,\tau_e}^{l,x,m} \end{bmatrix}, \tag{13}$$

where $N_{\mathcal{T}_c}$ is the number of the total discretized elements in subdomain $\mathcal{T}_c$,

$$m_{i\phi_j}^{l,x,m}=\begin{cases} \int_{\tau_e}\{C_{i,\nabla\phi_i}^{x,m}\nabla\upsilon_p^l\cdot\nabla\upsilon_q^l+C_{i,\phi_i}^{x,m}\upsilon_p^l\upsilon_q^l\}\mathrm{d}\mathbf{r}-\int_{\partial\tau_e}C_{i,\nabla\phi_i}^{x,m}f_{\mathbf{v}\cdot\phi_i^{x,m}}(\upsilon_p^l)\upsilon_q^l\mathrm{d}\mathbf{r} & \text{if} \quad i=j \\ \int_{\tau_e}C_{i,\phi_j}^{x,m}\upsilon_p^l\upsilon_q^l\mathrm{d}\mathbf{r}-\int_{\partial\tau_e}C_{i,\nabla\phi_i}^{x,m}f_{\mathbf{v}\cdot\phi_i^{x,m}}(\upsilon_p^l)\upsilon_q^l\mathrm{d}\mathbf{r} & \text{if} \quad i\neq j \end{cases}$$

and

$$\begin{cases} b_{i,\phi_i}^{l,x}=\int_{\partial\tau_e}C_{i,\nabla\phi_i}^{x}f_{S_i}(S_i)\upsilon_p^l\mathrm{d}\mathbf{r} \\ b_{i,\phi_i}^{l,m}=\int_{\tau_e}\frac{Q\mu_a^{xf}}{1+i\omega\tau}\phi_i^{l,x}\upsilon_p^l\mathrm{d}\mathbf{r} \end{cases}.$$

τ_e and $\partial\tau_e$ are the basic volumetric and surface elements of the mesh and belong to the respective subdomain in parallel implementation. After assembling all the submatrices on element τ_e, we obtain

$$\begin{bmatrix} M_{1\phi_1}^{\mathcal{T}_c,l,x,m} & M_{1\phi_2}^{\mathcal{T}_c,l,x,m} & \cdots & M_{1\phi_{(N+1)/2}}^{\mathcal{T}_c,l,x,m} \\ M_{2\phi_1}^{\mathcal{T}_c,l,x,m} & M_{2\phi_2}^{\mathcal{T}_c,l,x,m} & \cdots & M_{2\phi_{(N+1)/2}}^{\mathcal{T}_c,l,x,m} \\ \vdots & \vdots & \vdots & \vdots \\ M_{(N+1)/2\phi_1}^{\mathcal{T}_c,l,x,m} & M_{(N+1)/2\phi_2}^{\mathcal{T}_c,l,x,m} & \cdots & M_{(N+1)/2\phi_{(N+1)/2}}^{\mathcal{T}_c,l,x,m} \end{bmatrix}\begin{bmatrix} \phi_1^{\mathcal{T}_c,l,x,m} \\ \phi_2^{\mathcal{T}_c,l,x,m} \\ \vdots \\ \phi_{(N+1)/2}^{\mathcal{T}_c,l,x,m} \end{bmatrix}=\begin{bmatrix} b_1^{\mathcal{T}_c,l,x,m} \\ b_2^{\mathcal{T}_c,l,x,m} \\ \vdots \\ b_{(N+1)/2}^{\mathcal{T}_c,l,x,m} \end{bmatrix}. \tag{14}$$

In contrast to fixed or uniformly refined meshes, adaptively refined meshes require an *a posteriori* error estimation and the processing of hanging nodes. *A posteriori* error estimators decide which element should be refined or coarsened based upon the current solution. In parallel mode, the local error indicators are suitable because they reduce communications between processors. In this application, the gradient-jump error indicator is applied (Kelly *et al* 1983). For the SP_N, the local jump indicator for element τ_e is defined as (Kirk 2007)

$$\eta_{\tau_e}^{x,m}=\sum_{i=1}^{N}w_i\left(\frac{h_{\tau_e}}{24}\int_{\partial\tau_e}|R_{i,\tau_e^{x,m}}|^2\mathrm{d}\mathbf{r}\right)^{1/2}, \tag{15}$$

where w_i is a weighted factor corresponding to ϕ_i, and R_{i,τ_e} is the local residual for ϕ_i, which is defined by

$$R_{i,\tau_e}^{x,m}=\begin{cases} f_{\mathbf{v}\cdot\phi_i^x}(S)-\mathbf{v}_{\tau_e}\cdot\nabla\phi_i^{l,x,m} & \text{if} \quad \partial\tau_e\in\partial\Omega \\ \frac{1}{2}\mathbf{v}_{\tau_e}(\nabla\phi_i^{l,x,m}|\tau_{e_q}-\nabla\phi_i^{l,x,m}|\tau_{e_q}) & \text{if} \quad \partial\tau_e\in\tau_{e_p}\cap\tau_{e_p} \end{cases}. \tag{16}$$

$\mathbf{v}_{\tau_e}$ is the outward unit normal for element τ_{e_p} and h_{τ_e} is the diameter of τ_{e_p}. Using $\eta_{\tau_e}^{x,m}$, a statistical strategy is used to decide the proportion of refined and coarsened elements (Carey 1997) by computing the mean (m) and standard deviation (σ) of the distribution as an indictor for adaptive refinement or coarsening. The refinement and coarsening ratios (γ_r and γ_c) are set to select elements. By judging whether the log-error of one element is higher than ($m + \gamma_r \sigma$), or lower than ($m-\gamma_c\sigma$), the element is either refined or coarsened. When coarsening an element, only the refined elements are operated upon.

Since the hanging node constraint needs to consider specific elements in geometric method processing, the algebraic constraint method is selected to deal with hanging nodes (Carey 1997). Adaptive mesh evolution brings new challenges for balancing computational burden across partitioned domains. Imbalance deteriorates parallel performance and dynamic repartitioning of the mesh is indispensable for balancing computational burden. A *k*-way partitioning method is used to perform the partitioning after mesh refinement (Karypis and Kumar 1998). The reader is referred to Lu and Chatziioannou (2009) for details.

2.3. Time-resolved tetrahedron-based Monte Carlo fluorescence simulation

MC methods provide ground truth to evaluate and validate photon migration simulations. The need to simulate illumination patterns that have been demonstrated to improve reconstructions (Joshi *et al* 2006) and incorporate time dependence (Sevick-Muraca *et al* 1997, Li *et al* 1998, Godavarty *et al* 2004, Patwardhan *et al* 2005) while providing comparable domains for validating FEM solutions of complex geometries requires new MC solvers. To fully validate the SP_N approximations for our parallel FEM solver, we develop a time-resolved MC fluorescence simulator (TR-TIM-OS) based on a tetrahedron-based inhomogeneous MC optical simulator (TIM-OS) (Shen and Wang 2010).

2.3.1. Arbitrary shaped source settings and photon sampling—Triangular and tetrahedral elements have become popular in numerical computation, especially in numerical computation, because of their ability to describe complex geometries. Tetrahedron-based MC photon simulation facilitates validation of complex geometries and patterned illumination sources that require triangular and tetrahedral elements (Shen and Wang 2010). In fluorescent photon MC, there are two manners to initiate photon trajectories: (i) through external illumination of excitation photons and (ii) through internal generation of emission photons.

On the boundary of a domain, a triangle is the basic element describing the surface. In order to set arbitrary-shaped area illumination E_{ai}, a group of triangles ($G_{\partial\tau}^x=\{\partial\tau_1^x,\ldots,\partial\tau_i^x,\ldots,\partial\tau_{N_{\partial\tau}^x}^x\}$) at any position of the surface can be selected. In order to simulate the spatially uniform photon illumination when the area of the selected triangles is calculated, a uniform random number generator can be used to randomly select one from all the triangles depending on their areas. In a selected triangle, the position of the sampled point obeying the uniform random distribution is given by (Turk 1990)

$$p_{\partial\tau_i}^{x,rd}=p_{\partial\tau_i}^1*rd_1+p_{\partial\tau_i}^2*rd_2+p_{\partial\tau_i}^3*rd_3, \tag{17}$$

where rd_1 and rd_2 are the random number obeying a uniform distribution. If the sum of rd_1 and rd_2 is greater than '1.0', two new random numbers for them are regenerated. Conversely, $rd_3 = 1 - rd_1 - rd_2$. The emitting direction $\mathbf{v}_{\partial\tau_i}^{rd}$ ($\mathbf{v}_{\partial\tau_i}^{rd} \cdot \mathbf{v}_{\partial\tau_i} < 0$) of the photon can be uniformly sampled.

Since the volumetric domain is discretized using tetrahedral elements, a group of tetrahedra ($G_\tau^{om} = \{\tau_1^{om}, .., \tau_i^{om}, \ldots, \tau_{N_\tau^{om}}^{om}\}$) can be selected as volumes containing fluorophores of uniform distribution that can be sites for generation of fluorescent photons. Similar to the method for simulating excitation area illumination, any τ_i^{om} can be selected randomly. The position $p_{\tau_i}^{m,rd}$ of the generated emission photon can be obtained randomly and quickly using the algorithm in Rocchini and Cignoni (2000). The emitting direction of the emission photon can then be uniformly sampled over the whole solid angle.

2.3.2. Photon tracking—Once the initial excitation or emission photon generation is simulated as described above, trajectories are simulated using conventional MC techniques (Wang *et al* 1995, Boas *et al* 2002) where the weight of each photon is set to '1.0' and attenuated depending upon the length of a step; each step length is sampled from

$$s^{x,m} = \frac{-\ln rd_s}{\mu_a^{x,m} + \mu_s^{x,m}}, \tag{18}$$

where rd_s is a uniform random number in [0, 1]. The corresponding time traveled is calculated from

$$\Delta t^{x,m} = \frac{s^{x,m}}{c_b}. \tag{19}$$

When an emission photon is generated, the photon travel time is increased by $(-\ln(rd_l)\tau)$ due to the fluorescence lifetime, where rd_l is similar to rd_s. At each step, the position, weight and accumulated travel time are recorded. In MC simulation using tetrahedron-based discretized domains, a data structure is designed to record the element adjacent information. When the photon trajectory occurs over two or even several tetrahedra, the photon trajectory can also be quickly localized through the established element adjacent information. Preliminary tests have shown that tetrahedron- and analytic geometry-based MC simulation have comparable simulation time (Shen and Wang 2010), although for validation work, simulation time is not as critical as is for FEM simulation. After setting the time step Δt_{MC} and the total photon traveling time T_{MC}^x and T_{MC}^{om} for excitation and emission procedures, respectively, the absorbed photon weight over time can be recorded before it is terminated.

2.3.3. Convolution-based emission simulation—In the MC simulation employed, simulation of excitation and emission photon distributions are performed separately. After simulating the temporal excitation, the fluence distribution over time is obtained within the whole simulation domain. $\varphi_{\tau_i}^x(t_p), t_p \in [1, N_t^x]$ is used to describe the fluence in the tetrahedral element τ_i^{om}. If $G_{\partial\tau}^m = \{\partial\tau_1^m, \ldots, \partial\tau_j^m, \ldots, \partial\tau_{N_{\partial\tau}^m}^m\}$ describes a group of triangles for the surface measurement domain, then to each τ_i^{om} and $\partial\tau_j^m$, the time-resolved emission surface fluence

$\varphi^{om}_{\tau_i^{om}\to\partial\tau_j^m}(t_q), t_q \in [1, N_t^{om}]$ is obtained in the emission simulation. The final emission fluence $\varphi^m_{\partial\tau_j^m}(t_r), t_r \in [1, N_t^x + N_t^{om} - 1]$ on the surface triangle $\partial\tau_j^m$ can be computed from

$$\varphi^m_{\partial\tau_j^m}(t_r) = \sum_{t_p=1}^{N_t^x} \varphi^x_{\tau_i}(t_p)\varphi^{om}_{\tau_i^{om}\to\partial\tau_j^m}(t_r - t_p). \tag{20}$$

With $\varphi^x_{\tau_i}(t_p), \varphi^{om}_{\tau_i^{om}\to\partial\tau_j^m}(t_q)$ and $\varphi^m_{\partial\tau_j^m}(t_r)$, the corresponding amplitude and phase shift can be determined from the discrete Fourier transform of $\varphi^m_{\partial\tau_j^m}(t_r)$ when the specific modulated frequency ω is selected (Pan *et al* 2007). The convolution approach dramatically speeds upon time-dependent MC simulation of emission.

3. Simulations

In order to demonstrate the performance of the SP_N approximations, the in-house code was evaluated (SP_1(i.e. the diffusion approximation), SP_3 and SP_7) for performance and compared to MC for validation. Currently, many open-source, high-quality software packages have been developed to meet the need of FEM-based simulation. In our application, libMesh was selected as the basis development environment (Kirk *et al* 2006). LibMesh provides almost all of the components used in parallel PDE-based simulation with unstructured discretization. We used PETSc developed by Argonne National Laboratory (ANL) to solve the linear systems in parallel mode (Balay *et al* 2001) and METIS (Karypis and Kumar 1998) to dynamically partition the whole domain in libMesh using the *k*-way partitioning algorithm. The time-resolved tetrahedron-based MC program, that is TR-TIM-OS, was written in C/C++ (Intel MKL 2009). All the simulations were performed on a cluster of eight nodes (eight CPU cores of 3.0 GHz and 16 GB RAM at each node).

3.1. Validation of SP_N approximations with Monte Carlo simulation

The validation studies were performed using a simulated cylindrical phantom of 12.5 mm radius and 25.0 mm height. The phantom was simulated to contain a single spherical fluorescent heterogeneity and a second non-fluorescent inclusion (figures 1(a) and (b)). The center of the phantom is located at the origin of the Cartesian coordinate. The phantom was discretized into a tetrahedron-based volumetric mesh with approximately 5900 nodes and the average element diameter of 1.2 mm. This mesh was used in the SP_N- and *MC*-based simulations. The range of the launched photon numbers was from 10^7 to 10^8. With the increase of the absorption coefficient, the number of launched photons was increased to reduce simulated Poisson noise. A fluorescent spherical volume with 1.0 mm radius was simulated at the half-radius position (the center: (− 6.25, 0.0, 0.0)) as the single fluorescent domain. An area located at the height of 4.0 mm along the Z-axis subtending a circumferential angle of 11.2° was used as the uniform illumination area with its center along the negative *x*-axis. The absorption and scattering coefficients of the phantom were set to 0.005 mm^{-1} and 5.0 mm^{-1}, respectively. The anisotropic factor and refractive index were 0.9 and 1.33, respectively. The absorption coefficient, lifetime and quantum efficient (QE) of the fluorophore were set to 0.0147 mm^{-1}, 1.0 ns, and 0.016 consistent with available near-infrared fluorophores. The goal of fluorescence molecular imaging/tomography is to acquire the quantitative information of the fluorophores in the *in vivo* animal and human body; the two parameters collected were the excitation photon fluence distribution ($\varphi^x(\mathbf{r}), r \in \Omega$) in the body and the outgoing emission photon fluence ($J_m^+(\mathbf{r}), r \in \partial\Omega$).

The comparison results of J_m^+ are shown in figure 2 for a modulation frequency of 100 MHz. The amplitudes obtained from SP_N approximations and MC simulation were normalized with the average values of SP_7 and MC methods, respectively. The absolute phase shift was used for the comparison. In order to demonstrate the difference between SP_N approximations and MC simulation, their amplitude ratios and phase shift errors were calculated using ($A_{SP_N}^{\text{norm}}/A_{\text{MC}}^{\text{norm}}$) and ($P_{SP_N} - P_{\text{MC}}$), respectively. $A_{SP_N}^{\text{norm}}$ and $A_{\text{MC}}^{\text{norm}}$ are the normalized SP_N and MC amplitude; P_{SP_N} and P_{MC} are the corresponding absolute phase shift. Due to the effect of the Poisson noise of the MC simulation in J_m^+, the values of the points far from the fluorophore have somewhat larger errors than those close to the fluorophore. However, the amplitude ratios and phase errors between several SP_N approximations and MC are close, showing the accuracy of the in-house codes.

3.2. Performance of SP_N approximations

3.2.1. With varying ratios of μ_s' to μ_a—The performance evaluation of the SP_N approximations in fluorescence molecular imaging was first performed with different ratios of μ_s' to μ_a. When the absorption coefficient of the phantom was adjusted to 0.05 mm^{-1} with other parameters unchanged from those used in the accuracy validation, the comparison of J_m^+ and φ^x between several SP_N approximations and MC was computed as shown in figures 3(a) and (b), respectively. At the ratio of μ_s' to μ_a of 10, the difference of the amplitude ratios and phase errors between SP_1, SP_3 and SP_7 becomes distinct as compared to when the ratio was set to 100 (figure 2). With the increase of the distance from the illumination area, the phase errors of φ^x gradually become large (~1.0°). Note that the simulated amplitudes near the source domain from all SP_N approximations are inaccurate, resulting in the inaccuracy of the normalized amplitude ratios. The distance from the illumination area where this inaccuracy predominates extends about 3.0 mm in this case. When the amplitudes were re-normalized using the average values of φ^x that did not include values within this distance from the source, better accuracy of the SP_N-based amplitudes occurs (figure 3(b)). In these simulations, the errors arise from both model mismatch and discretization. To further confirm the performance of SP_N approximation in the near-source domain, a fine mesh consisting of approximately 46 000 nodes and having an average element length of 0.55 mm was used. Upon setting the ratios of μ_s' to μ_a to 10.0 and 2.0 and launching 10^8 and 3×10^8 photons, respectively, we observe that the errors are reduced as shown in figures 4(a) and (b). Although the phase shift errors are reduced and the amplitude ratio ranges are closer to '1.0', the error and ratio trends are consistent with those using the coarse mesh. Furthermore, the inaccuracy of SP_N approximation in the near-source domain remains.

When the absorption coefficient of the phantom was set to 0.25 mm^{-1} (and the ratio of μ_s' to μ_a is 2.0), the advantages of the high-order SP_N approximations become more distinct as shown in figures 3(c) and (d). In this case, the amplitude and phase shift of J_m^+ and φ^x, computed from SP_3 and SP_7, contain the maximal amplitude ratio and phase errors that differ from MC by a factor of 0.4 and 2.0°, respectively. The comparable errors between SP_1 and MC are 0.9 and 4.0°. The corresponding differences of φ^x between DA and high-order SP_N approximations are also distinct as shown in figure 3(d). The inaccuracy becomes worse regarding SP_N approximations with the increased distances from the fluorophore and illumination area. Note that near the source, the distance in which φ^x inaccuracy occurred did not change when the absorption coefficient of the phantom was adjusted from 0.05 mm^{-1} to 0.25 mm^{-1}.

3.2.2. With varying modulation frequencies—Although 100 MHz is the optimal modulation frequency for experimental measurements (Thompson and Sevick-Muraca 2003), higher modulation frequencies of 500 and 1000 MHz were considered to evaluate the

performance of high-order SP_N approximations. Figure 5 shows the comparison of SP_N approximations and MC simulations when the absorption and scattering coefficients of the phantom were fixed to 0.05 and 5.0 mm^{-1}, respectively. Similar accuracies of the excitation and emission amplitude at 100 MHz cases were obtained. However, the diffusion equation has inaccurate excitation and emission phase when compared with high-order SP_N approximations. With the increase of the modulation frequency, the diffusion inaccuracy becomes worse. For J_m^+, the maximal phase errors of SP_3 and SP_7 relative to MC are 2.0 and 4.0° at 500 and 1000 MHz, respectively. However, the counterparts of the diffusion equation reach 6.0 and 12.0°.

3.2.3. With inclusions of high absorption and void-like optical characteristics—

In practice, small animal fluorescence molecular imaging encounters organs of varying optical properties. The performance evaluation in heterogeneous domains is important. A cylindrical phantom with 2.0 mm radius and 20.0 mm height was simulated within the cylindrical homogeneous phantom. Its center was co-located with that of the homogeneous phantom. The discretized volumetric mesh is shown in figure 1(b), consisting of 6162 nodes. The same fluorophore properties with the validated homogeneous phantom case were used in this evaluation. The optical properties of the surrounding continuous volume were set to 0.05 (μ_a) and 5.0 mm^{-1} (μ_s), respectively. The optical properties of the inclusion were set to 0.25 (μ_a) and 5.0 mm^{-1} (μ_s), to simulate the high-absorption domain. As shown in figures 6(a) and (b), there is little effect of the high-absorption domain in values of J_m^+ computed from the SP_N approximations. However, φ^x of several SP_N approximations are inaccurate in the simulated phantom containing the high-absorption region, significantly affecting the quantitative information acquisition of the fluorophore. Note that there is little effect in the phase shift compared with the emission amplitude.

For the void-like case, the simulated inclusion was set as a low-scattering domain with a scattering coefficient of 0.1 mm^{-1} and the high ratio of μ_s' and μ_a equal to 20.0. The comparison of MC and SP_N approximations of J_m^+ and φ^x is shown in figures 6(c) and (d). Similar to the high-absorption inclusion, low-scattering inclusions appreciably impact J_m^+ even though φ^x is inaccurate compared to MC simulation.

4. Evaluation of the parallel adaptive finite element strategy on a simulated mouse

As the final evaluation of the proposed algorithm, the microMRI-based mouse volume (MOBY) (Segars *et al* 2004) was investigated for accuracy and computational performance. Amira 5.2 (Visage Imaging, Inc., San Diego, CA) was used to obtain the discretized mesh of MOBY. The coarse and fine meshes, consisting of approximately 21 000 and 230 000 discretized points, respectively, were generated for adaptive mesh evolution and the acquisition of the precise solution. Most organs were depicted in the discretized mesh as described along with assigned optical properties in table 1, reproduced from Alexandrakis *et al* (2005). To represent a fluorescent heterogeneity, a cubic domain with volume of 15.6 mm^3 was simulated within the liver. The optical parameters of the fluorophore were the same with those used in the cylindrical phantom. The illumination area was simulated as a triangular element near the *x*-axis on the mouse surface. In order to observe the performance of the adaptive mesh evolution as a function of SP_N, the solutions were obtained from the SP_3 and SP_7 approximations of the excitation light only. Because emission and excitation solutions are solved on independently adapted meshed and require accurate interpolation schemes (for example see Lee *et al* (2008)), we focus only on the effect of SP_N approximation order on adaptive meshes in the simulation precision. Future work will address independently adapted meshing.

The dynamic mesh partitioning and adaptive mesh evolution are shown in figure 7 when ten domains and ten CPUs were used in the parallel adaptive simulation. To guarantee the same number of the final discretized points in SP_3- and SP_7-based simulation, the refinement ratio γ_r was set to 99.9% and 99.91%, respectively, and both of the coarsening ratios γ_c were set to 0.0%. Upon comparing the initial partitioned mesh and the counterparts after the first and third adaptive mesh refinements (figure 7), one finds that the subdomains for CPUs were almost totally different due to the adaptive mesh evolution. If the initial partitioning mesh was used for the entire simulation, the load imbalance would significantly impair the simulation performance. It is noteworthy that because the larger errors exist in the proximity of the illumination area, mesh refinements were performed primarily in the vicinity of the triangular surface element.

After the SP_3-, SP_7- and MC-based simulation results were acquired on the fine mesh of the MOBY, the amplitude and phase shift profiles of φ^x along the X-axis transecting the fluorophore domain were obtained by the interpolation. The relative errors of the normalized amplitude and phase shift were calculated using $|A^{\text{norm}}_{SP_N} - A^{\text{norm}}_{MC}|/A^{\text{norm}}_{MC}$ and $|P\,SP_N - P_{MC}|/|P_{MC}|$ as shown in figure 8. To remove the effect of the inaccuracy of SP_3 and SP_7 in the near-source domain, the φ^x values within the range of 3.0 mm far from the illumination were not considered in the comparisons. Compared to the solution on the fine mesh, the solutions of the excitation amplitude and phase shift of SP_3 and SP_7 close to the illumination are significantly improved due to the adaptive mesh evolution. Note that there are several spikes in the comparisons. We believe the spikes are from the poor discretization and element quality since they are not observed from the solution on the fine mesh.

To further observe the performance of the proposed algorithm, the computational time as a function of CPUs is shown in figure 9. For the SP_3- and SP_7-based simulations on the adaptive and fixed fine meshes, the parallel implementation significantly improves the simulation speed although the simulation is not always accelerated with the increasing CPU number. The maximal acceleration ratios for fixed fine meshes were 1.27 and 2.31 for SP_3 and SP_7, respectively. The maximal acceleration ratios for adaptively refined meshes were 2.93 and 4.13 for SP_3 and SP_7, respectively. These results show that the acceleration ratio is more positively impacted by adaptive mesh evolution for SP_7 than SP_3. However, higher order approximations take more CPUs (10 and 18 CPUs for SP_3 and SP_7, respectively).

The computational time of several modules that perform specific computational tasks, *matrix assembly*, *mesh communication*, *mesh partitioning*, *mesh adaptive*, *error estimation* and *solver*, were considered to analyze performance bottleneck. Figures 9(b) and (c) illustrate the computational time as a function of number of CPUs for SP_3 and SP_7, respectively. Although the time costs of several modules (*matrix assembly*, *error estimation* and *solver*) are quickly reduced at the beginning, the improvement of the time cost decreases after an optimal CPU number. In contrast, *mesh communication* becomes worse with the increased number of CPU due to the more frequent communication between CPUs. Furthermore, figure 9(d) shows the percentage of several modules in the total simulation time. *Mesh communication* and *solver* are the major time-consuming modules especially with the increase of the approximation degree. Significant improvement can be obtained by the acceleration of *solver*.

5. Summary and conclusion

Herein, a parallel adaptive finite element simulation algorithm is developed with the radiative-transfer-based model for frequency domain fluorescence molecular imaging. To demonstrate the performance of high-order SP_N approximations, the time-resolved tetrahedron-based Monte Carlo fluorescence simulator is developed, suitable for complex heterogeneous geometries and arbitrary-shaped illumination. The comparison results show that high-order

SP_N approximations may obtain more precise simulation in the high-absorption and high-frequency cases compared with the popular diffusion approximation. The strategy of the parallel adaptive mesh evolution further accelerates the simulation and improves the simulation precision especially when higher order SP_N approximations are applied. The proposed simulation algorithm provides a possible solution for fast and quantitative fluorophore reconstruction for fluorescence molecular tomography at the whole-body small animal level.

Although the radiative transfer equation can provide more accurate solutions, the cost may prevent its use within iterative inverse solutions. For accurate quantitation in drug discovery, suitable high-order approximations may be necessary. As a consequence, optimizing performance of higher order approximations become necessary in order to realize reconstruction accuracy. This paper systematically demonstrates accuracy improvements compared with the diffusion equation and developed Monte Carlo methods. The time cost of SP_7 approximation makes the SP_3 approximation an optimal choice for conditions in which small animal imaging is conducted. However, the poor performance of SP_N approximations in near-source and void-like regions makes the development and investigation of more advanced high-order approximations necessary.

Precise and fast simulation can be obtained using a fully parallel adaptive mesh evolution strategy. The performance evaluation shows that the time improvement of higher order SP_N approximations obtained from the proposed algorithm becomes more distinct compared with sequential implementation, providing a powerful computational platform for radiative-transfer-based simulation. However, the distributed memory-based parallel simulation exhibits a performance bottleneck especially when a great number of CPUs are used. With the increase of the approximation degree of radiative-transfer-based model, it is necessary to obtain optical simulation performance by increasing the CPU number. The development of current multi-core techniques makes the hybrid threaded-MPI parallel mode possible, potentially improving the simulation performance for the high-order radiative-transfer-based model. Module *solver* becomes a time-consuming phase especially for higher order approximation. Note that the acceleration becomes slow when the CPUs reach a certain number. To improve the parallel simulation performance, more advanced preconditioners and iterative techniques need to be investigated.

In conclusion, we have developed a fully parallel adaptive finite element algorithm for fluorescent photon propagation simulation using high-order radiative-transfer-based models. The fully performance evaluations show the advantages and limits of SP_N approximations and the developed parallel simulation framework. Optimal improvements can be further investigated in future research. Currently, using dual-labeled near-infrared fluorescence and PET traces, we are developing methods to assess the quantitative algorithm by comparing it to established PET.

Acknowledgments

We thank Dr Tianshu Pan for the significant discussion on the frequency-domain problem and Robert Haacke for his assistance in the Cluster. We are grateful to the development teams of libMesh and PETSc for discussions. This work is supported by NIH R01CA135673 and U54CA136404 (Sevick), and NIH R01HL098912 (Wang).

Nomenclature

$\boldsymbol{\Omega}$, $\partial\boldsymbol{\Omega}$	domain and its boundary
$\mathbf{r}$	position vector
$\hat{\mathbf{s}}$, $\hat{\mathbf{s}}'$	outgoing and incoming directions of photons

ω	modulation frequency
$\psi^{x,m}$	excitation (^{x}) and emission (^{m}) radiances
$\mu_a^{x,m}, \mu_s^{x,m}, g$	absorption and scattering coefficients, and anisotropy factor of the domain at excitation and emission wavelengths
μ_a^{xf}	absorption coefficient of the fluorophore
c_b	light speed in the domain Ω
$p(\cdot)$	scattering phase function
Q,τ	quantum efficiency and lifetime of the fluorophore
$\cos\theta$	scattering angle
$\varphi^{x,m}$	excitation and emission fluence
n_b, n_m	refractive indices of the domain Ω and the medium
S	illumination source
$R(\cdot)$	reflectivity ratio
$\theta_b, \theta_m, \theta_c$	incidence, transmission and critical angle
$J^+_{x,m}$	exiting partial current at excitation and emission wavelengths
γ_n, ϕ_n	*Legendre moments* of ψ and *composite moments* of γ_n
$C^{x,m}_{i,\nabla\phi_i}, C^{x,m}_{i,\phi_j}$	coefficients of SP_N approximations at excitation and emission wavelengths
$C^x_{i,S}$	coefficients of illumination source of SP_N approximations
$C^{b,x,m}_{i,\nabla\phi_j}, C^{b,x,m}_{i,\nabla\phi_j}$	coefficients of boundary conditions at excitation and emission wavelengths
$\mathcal{T}$, $\mathcal{T}_c$	volumetric mesh and its subdomain
N_c, N_p, $N_{\mathcal{T}_c}$	number of CPUs, nodes of the mesh, elements in $\mathcal{T}_c$
$\tau_e, \partial\tau_e$	volumetric and surface elements
$\phi^{l,x,m}_{i,p}$	value at node p at the l-th mesh
υ^l_p	basis function in FEM
$m^{l,x,m}_{i\phi_j}, b^{l,x,m}_{i,\phi_i}$	submatrix and subvector at τ_e
$M^{\mathcal{T}_c,l,x,m}_{i\phi_j}, b^{\mathcal{T}_c,l,x,m}_i$	submatrix and subvector at $\mathcal{T}_c$
$\eta^{x,m}_{\tau_e}$	error indicator
$w_i, R^{x,m}_{i,\tau_e}$	weighted factor and local residual
γ_r, γ_c	refinement and coarsening ratios
$G^x_{\partial\tau}, G^m_{\partial\tau}, G^{om}_{\tau}$	group of triangles for illumination and emission measurements, group of tetrahedra for fluorephore
rd_i	uniformly random number
$p^{x,rd}_{\partial\tau_i}$	sampled point on the surface for excitation

$\boldsymbol{s^{x,m}}$	step size of photon trajectory
$\boldsymbol{\Delta t^{x,m}}$	traveling time corresponding to $s^{x,m}$
T^{x}_{MC}, T^{om}_{MC}	simulation time for excitation and emission wavelengths
$\boldsymbol{\Delta t_{MC}}$	$\Delta t^{x,m}$, time step and travel time of photons
$\varphi^{x}_{\tau_i}(\cdot), \varphi^{m}_{\partial\tau^{m}_{j}}(\cdot)$	time-resolved excitation and emission fluences
$\varphi^{om}_{\tau^{om}_{i}\to\partial\tau^{m}_{j}}(\cdot)$	time-resolved artificial emission fluence

References

Alexandrakis G, Rannou FR, Chatziioannou AF. Tomographic bioluminescence imaging by use of a combined optical-PET (OPET) system: a computer simulation feasibility study. Phys Med Biol 2005;50:4225–41. [PubMed: 16177541]

Balay, S.; Buschelman, K.; Gropp, WD.; Kaushik, D.; Knepley, MG.; McInnes, LC.; Smith, BF.; Zhang, H. PETSc web page. 2001. http://www.mcs.anl.gov/petsc

Boas D, Culver J, Stott J, Dunn A. Three dimensional Monte Carlo code for photon migration through complex heterogeneous media including the adult human head. Opt Express 2002;10:159–70. [PubMed: 19424345]

Carey, GF. Computational Grids: Generation, Adaptation, and Solution Strategies. London: Taylor and Francis; 1997.

Chaudhari AJ, Darvas F, Bading JR, Moats RA, Conti PS, Smith DJ, Cherry SR, Leahy RM. Hyperspectral and multispectral bioluminescence optical tomography for small animal imaging. Phys Med Biol 2005;50:5421–41. [PubMed: 16306643]

Cherry SR. *In vivo* molecular and genomic imaging: new challenges for imaging physics. Phys Med Biol 2004;49:R13–48. [PubMed: 15012005]

Cho J, Taschereau R, Olma S, Liu K, Chen Y, Shen C, van Dam R, Chatziioannou A. Cerenkov radiation imaging as a method for quantitative measurements of beta particles in a microfluidic chip. Phys Med Biol 2009;54:6757–71. [PubMed: 19847018]

Chu M, Vishwanath K, Klose AD, Dehghani H. Light transport in biological tissue using three-dimensional frequency-domain simplified spherical harmonics equations. Phys Med Biol 2009;54:2493–509. [PubMed: 19336841]

Cong W, Cong A, Shen H, Liu Y, Wang G. Flux vector formulation for photon propagation in the biological tissue. Opt Lett 2007;32:2837–9. [PubMed: 17909590]

Cong W, et al. Practical reconstruction method for bioluminescence tomography. Opt Express 2005;13:6756–71. [PubMed: 19498692]

Contag CH, Bachmann MH. Advances in bioluminescence imaging of gene expression. Annu Rev Biomed Eng 2002;4:235–60. [PubMed: 12117758]

Dehghani H, Davis SC, Jiang S, Pogue BW, Paulsen KD, Patterson MS. Spectrally resolved bioluminescence optical tomography. Opt Lett 2006;31:365–7. [PubMed: 16480210]

Gibson AP, Hebden JC, Arridge SR. Recent advances in diffuse optical imaging. Phys Med Biol 2005;50:R1–R43. [PubMed: 15773619]

Godavarty A, Eppstein M, Zhang C, Theru S, Thompson A, Gurfinkel M, Sevick-Muraca E. Fluorescence-enhanced optical imaging in large tissue volumes using a gain-modulated ICCD camera. Phys Med Biol 2003;48:1701–20. [PubMed: 12870578]

Godavarty A, Thompson A, Roy R, Gurfinkel M, Eppstein M, Zhang C, Sevick-Muraca E. Diagnostic imaging of breast cancer using fluorescence-enhanced optical tomography: phantom studies. J Biomed Opt 2004;9:488. [PubMed: 15189086]

Gu X, Kim H, Masciotti J, Hielscher A. A parallel reduced-space sequential-quadratic programming algorithm for frequency-domain small animal optical tomography. Proc SPIE 2009;7174:717406.

Haskell RC, Svaasand LO, Tsay T-T, Feng T-C, McAdams MS, Tromberg BJ. Boundary conditions for the diffusion equation in radiative transfer. J Opt Soc Am A 1994;11:2727.

Herschman HR. Molecular imaging: looking at problems, seeing solutions. Science 2003;302:605–8. [PubMed: 14576425]

Intel Math Kernel Library Reference Manual. 2009. http://software.intel.com/en-us/articles/intel-math-kernellibrary-documentation/

Ishimaru, A. Wave Propagation and Scattering in Random Media. Piscataway, NJ: IEEE Press; 1997.

Joshi A, Bangerth W, Sevick-Muraca EM. Adaptive finite element based tomography for fluorescence optical imaging in tissue. Opt Express 2004;12:5402–17. [PubMed: 19484100]

Joshi A, Bangerth W, Sevick-Muraca EM. Non-contact fluorescence optical tomography with scanning patterned illumination. Opt Express 2006;14:6516–34. [PubMed: 19516829]

Joshi A, Rasmussen J, Sevick-Muraca E, Wareing T, McGhee J. Radiative transport-based frequency-domain fluorescence tomography. Phys Med Biol 2008;53:2069–88. [PubMed: 18364555]

Karypis G, Kumar V. Multilevel k-way partitioning scheme for irregular graphs. J Parallel Distrib Comput 1998;48:96–129.

Kelly DWR, Gago JPDS, Zienkiewicz OC, Babuska I. *A posteriori* error analysis and adaptive processes in the finite element method: part i. Error analysis. Int J Numer Methods Eng 1983;19:1593–619.

Kirk B, Peterson JW, Stogner RH, Carey GF. libMesh: a C++ library for parallel adaptive mesh refinement/coarsening simulations. Eng Comput 2006;22:237–54.

Kirk, BS. PhD thesis. The University of Texas; Austin: 2007. Adaptive finite element simulation of flow and transport applications on parallel computers.

Klose A, Beattie B, Dehghani H, Vider L, Le C, Ponomarev V, Blasberg R. *In vivo* bioluminescence tomography with a blocking-off finite-difference SP_3 method and MRI/CT coregistration. Med Phys 2010;37:329. [PubMed: 20175496]

Klose AD, Larsen EW. Light transport in biological tissue based on the simplified spherical harmonics equations. J Comput Phys 2006;220:441–70.

Klose AD, Ntziachristos V, Hielscher AH. The inverse source problem based on the radiative transfer equation in optical molecular imaging. J Comput Phys 2005;202:323–45.

Kuo C, Coquoz O, Troy TL, Xu H, Rice BW. Three-dimensional reconstruction of *in vivo* bioluminescent sources based on multispectral imaging. J Biomed Opt 2007;12:024007. [PubMed: 17477722]

Lee J, Joshi A, Sevick-Muraca E. Fast intersections on nested tetrahedrons (FINT): an algorithm for adaptive finite element based distributed parameter estimation. J Comput Phys 2008;227:5778–98. [PubMed: 18688291]

Lewis, EE.; Warren, F.; Miller, J. Computational Methods of Neutron Transport. New York: Wiley; 1984.

Li X, Chance B, Yodh A. Fluorescent heterogeneities in turbid media: limits for detection, characterization, and comparison with absorption. Appl Opt 1998;37:6833–44. [PubMed: 18301500]

Lu Y, Chatziioannou A. A parallel adaptive finite element method for the simulation of photon migration with the radiative-transfer-based model. Commun Numer Methods Eng 2009;25:751–770. [PubMed: 20052300]

Lu Y, Douraghy A, Machado H, Stout D, Tian J, Herschman H, Chatziioannou A. Spectrally resolved bioluminescence tomography with the third-order simplified spherical harmonics approximation. Phys Med Biol 2009a;54:6477–93. [PubMed: 19820264]

Lu Y, Machado HB, Douraghy A, Stout D, Herschman H, Chatziioannou AF. Experimental bioluminescence tomography with fully parallel radiative-transfer-based reconstruction framework. Opt Express 2009b;17:16681–95. [PubMed: 19770883]

Lv Y, Tian J, Cong W, Wang G, Luo J, Yang W, Li H. A multilevel adaptive finite element algorithm for bioluminescence tomography. Opt Express 2006;14:8211–23. [PubMed: 19529195]

Massoud TF, Gambhir SS. Molecular imaging in living subjects: seeing fundamental biological processes in a new light. Genes Dev 2003;17:545–80. [PubMed: 12629038]

Pan T, Rasmussen J, Lee J, Sevick-Muraca E. Monte Carlo simulation of time-dependent, transport-limited fluorescent boundary measurements in frequency domain. Med Phys 2007;34:1298. [PubMed: 17500461]

Patwardhan S, Bloch S, Achilefu S, Culver J. Time-dependent whole-body fluorescence tomography of probe bio-distributions in mice. Opt Express 2005;13:2564–77. [PubMed: 19495147]

Rao, SS. The Finite Element Method in Engineering. Boston, MA: Butterworth-Heinemann; 1999.

Rasmussen J, Joshi A, Pan T, Wareing T, McGhee J, Sevick-Muraca E. Radiative transport in fluorescence-enhanced frequency domain photon migration. Med Phys 2006;33:4685. [PubMed: 17278821]

Rasmussen J, Tan I, Marshall M, Fife C, Sevick-Muraca E. Lymphatic imaging in humans with near-infrared fluorescence. Curr Opin Biotechnol 2009;20:74–82. [PubMed: 19233639]

Robertson R, Germanos M, Li C, Mitchell G, Cherry S, Silva M. Optical imaging of Cerenkov light generation from positron-emitting radiotracers. Phys Med Biol 2009;54:N355–65. [PubMed: 19636082]

Rocchini C, Cignoni P. Generating random points in a tetrahedron. J Graph Tools 2000;5:9–12.

Segars WP, Tsui BMW, Frey EC, Johnson GA, Berr SS. Development of a 4D digital mouse phantom for molecular imaging research. Mol Imaging Biol 2004;6:149–59. [PubMed: 15193249]

Sevick-Muraca E, Houston J, Gurfinkel M. Fluorescence-enhanced, near infrared diagnostic imaging with contrast agents. Curr Opin Chem Biol 2002;6:642–50. [PubMed: 12413549]

Sevick-Muraca E, Lopez G, Reynolds J, Troy T, Hutchinson C. Fluorescence and absorption contrast mechanisms for biomedical optical imaging using frequency-domain techniques. Photochem Photobiol 1997;66:55. [PubMed: 9230705]

Sevick-Muraca E, et al. Imaging of lymph flow in breast cancer patients after microdose administration of a near-infrared fluorophore: feasibility study. Radiology 2008;246:734. [PubMed: 18223125]

Shen H, Wang G. A tetrahedron-based inhomogeneous Monte Carlo optical simulator. Phys Med Biol 2010;55:947–62. [PubMed: 20090182]

Shu X, Royant A, Lin M, Aguilera T, Lev-Ram V, Steinbach P, Tsien R. Mammalian expression of infrared fluorescent proteins engineered from a bacterial phytochrome. Science 2009;324:804. [PubMed: 19423828]

Swartling J, Pifferi A, Enejder A, Andersson-Engels S. Accelerated Monte Carlo models to simulate fluorescence spectra from layered tissues. J Opt Soc Am A 2003;20:714–27.

Thompson A, Sevick-Muraca E. Near-infrared fluorescence contrast-enhanced imaging with intensified charge-coupled device homodyne detection: measurement precision and accuracy. J Biomed Opt 2003;8:111. [PubMed: 12542387]

Turk, G. Graphics Gems. New York: Academic; 1990. Generating random points in triangles; p. 28

Wang G, Li Y, Jiang M. Uniqueness theorems in bioluminescence tomography. Med Phys 2004;31:2289–99. [PubMed: 15377096]

Wang L, Jacques SL, Zheng L. —Monte Carlo modeling of photon transport in multi-layered tissues. Comput Methods Prog Biomed 1995;47:131–46.

Weissleder R. Molecular imaging: exploring the next frontier. Radiology 1999;212:609–14. [PubMed: 10478223]

Yuan Z, Hu X, Jiang H. A higher order diffusion model for three-dimensional photon migration. Phys Med Biol 2009;54:65–88. [PubMed: 19060361]

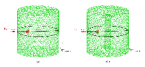

Figure 1.
The discretized meshes of the used phantoms. The black circles and lines are for comparisons of the exiting partial current J_m^+ and the fluence φ^x. The red solid spheres represent fluorescent heterogeneities and the cylindrical inclusion is also represented.

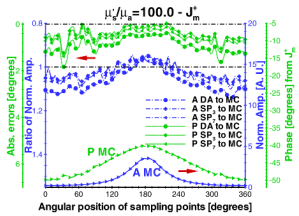

Figure 2.

Emission comparisons between the diffusion equation, Monte Carlo method and SP_N approximations in the phantom (figure 1(a)) where μ_a = 0.005 mm^{-1}, μ_s = 5.0 mm^{-1}, g = 0.9 and n_b = 1.33. The modulation frequency is 100 MHz. 'A * to MC' and 'P * to MC' denote the normalized amplitude ratios and the errors of the absolute phase shift between SP_N and MC. Two dash-dot lines are 0 degree (top) and the ratio of '1' (bottom).

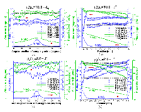

Figure 3.

Comparisons of J_m^+ ((a) and (c)) and φ^x ((b) and (d)) between the diffusion equation, Monte Carlo method and SP_N approximations in the homogeneous phantom when $\mu_s = 5.0\ \text{mm}^{-1}$, $g = 0.9$ and $n_b = 1.33$. The μ_s'/μ_a ratios of ((a) and (b)) and ((c) and (d)) are 10.0 and 2.0, respectively. The display settings are the same as those in figure 2.

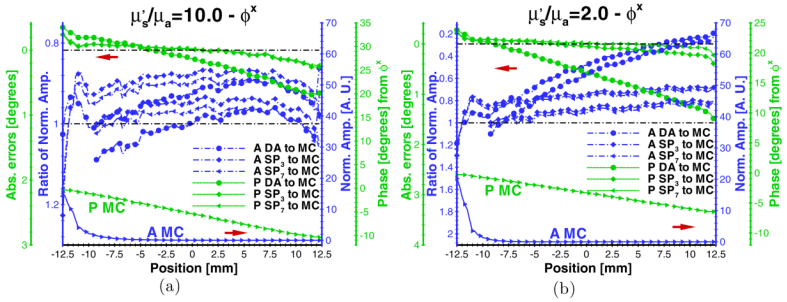

Figure 4.

Comparisons of φ^x between the diffusion equation, Monte Carlo method and SP_N approximations on the fine mesh of the homogeneous phantom when $\mu_s = 5.0\ \text{mm}^{-1}$, $g = 0.9$ and $n_b = 1.33$. The μ_s'/μ_a ratios of (a) and (b) are 10.0 and 2.0, respectively. The modulation frequency is 100 MHz. The display settings are the same as those in figure 2.

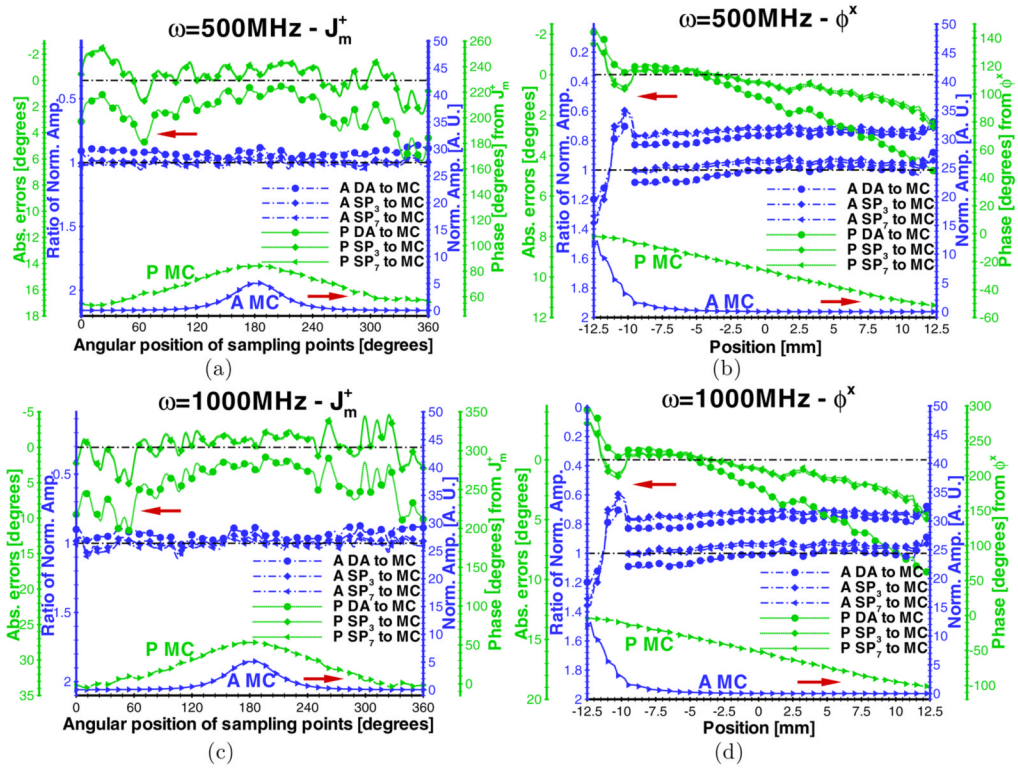

Figure 5.

Comparisons of J_m^+ ((a) and (c)) and φ^x ((b) and (d)) between the diffusion equation, Monte Carlo method and SP_N approximations in the homogeneous phantom when $\mu_a = 0.05\ \text{mm}^{-1}$, $\mu_s = 5.0\ \text{mm}^{-1}$, $g = 0.9$ and $n_b = 1.33$. The modulation frequencies are 500 MHz for (a) and (b) and 1000 MHz for (c) and (d). The display settings are the same as those in figure 2.

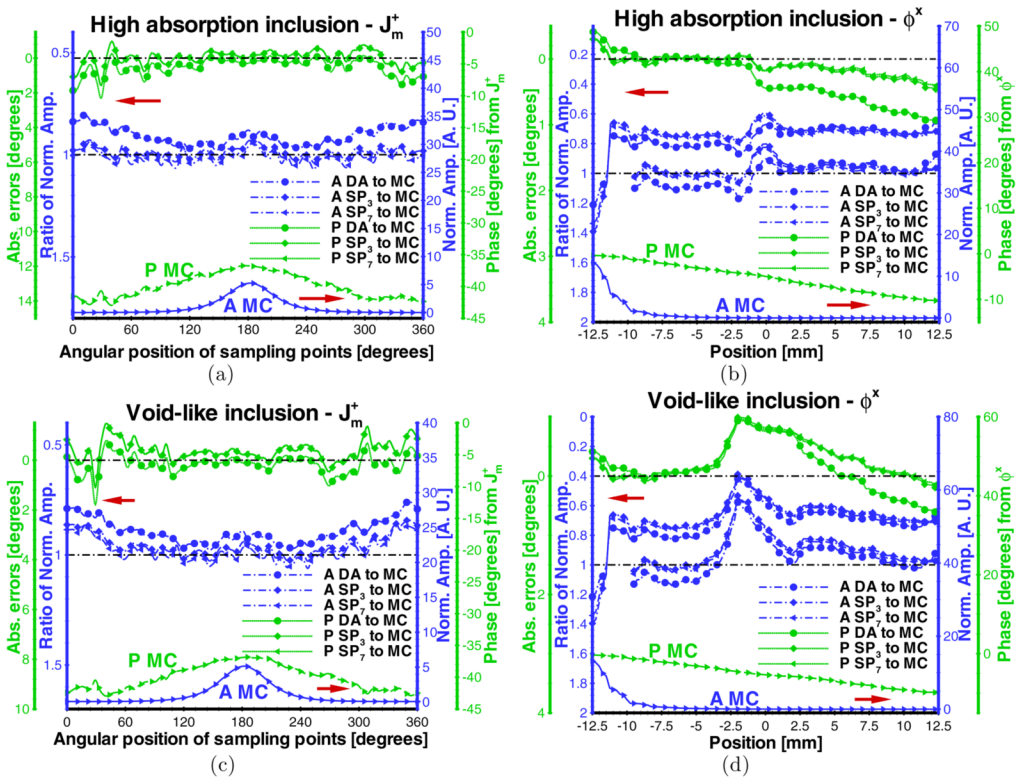

Figure 6.

Comparisons of J_m^+ ((a) and (c)) and φ_x ((b) and (d)) between the Monte Carlo method and SP_N approximations in phantoms containing high absorption and void-like inclusions. μ_a, μ_s, g, and n_b of the surrounding continuous volume of the phantom are fixed to 0.05 mm^{-1}, 5.0 mm^{-1}, 0.9, and 1.33, respectively. μ_a and μ_s of the small cylindrical inclusion are set to 0.25 mm^{-1} and 5.0 mm^{-1} (high absorption), and 0.005 mm^{-1} and 0.1 mm^{-1} (void-like), respectively. The modulation frequency is 100.0 MHz. The display settings are the same as those in figure 2.

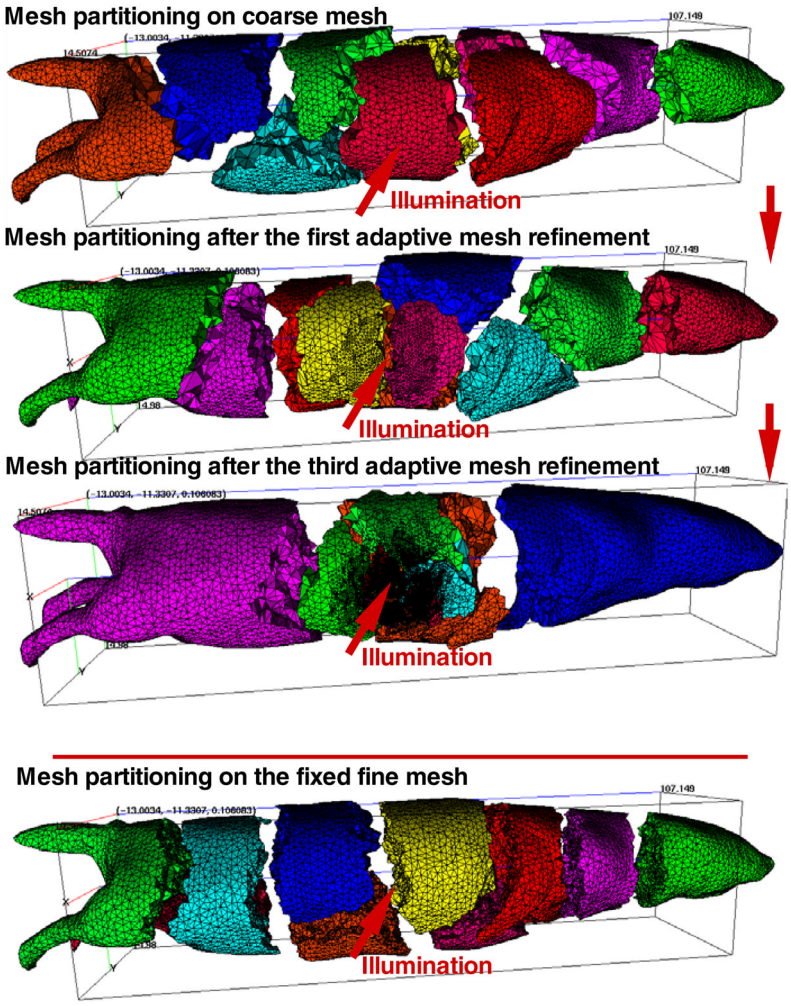

Figure 7.
Dynamic mesh partitioning and evolution and the fine mesh partitioning.

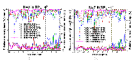

Figure 8.
Comparisons of φ^x between SP_3, SP_7 and the Monte Carlo method in the digital mouse phantom (MOBY). The modulation frequency is 100 MHz. 'A $SP_{3,7}$ (*) to MC' and 'P $SP_{3,7}$ (*) to MC' denote the relative errors of the excitation amplitude and phase shift on different fixed and adaptively refined meshes. The dash-dot rectangles are used to show the part of the significant error reduction due to the adaptive mesh evolution.

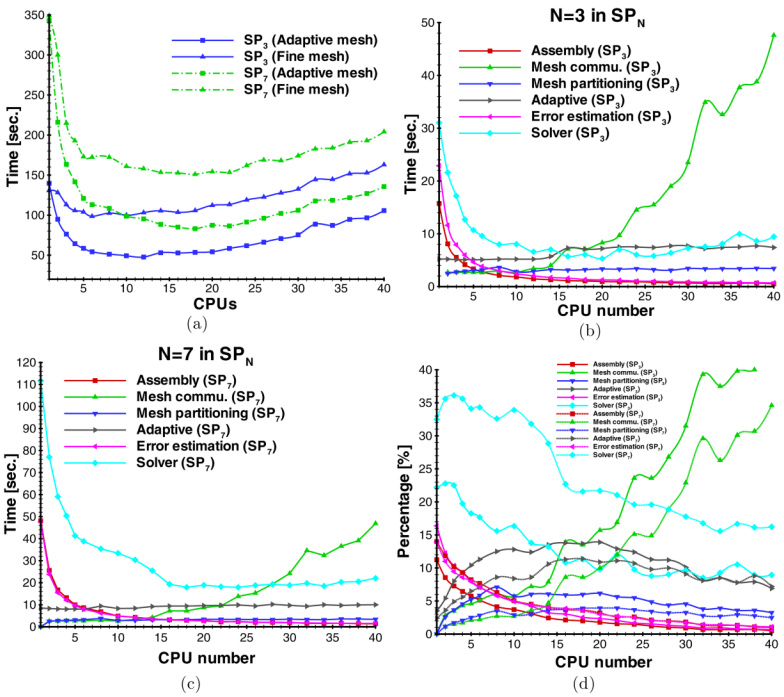

Figure 9.

Time analysis of SP_3- and SP_7-based simulation using the MOBY phantom. (a) The total cost time of the SP_3 and SP_7 approximations. (b) (SP_3) and (c) (SP_7) denote the cost time of the submodules of the parallel adaptive finite element simulation. (d) The time percentage of the submodules in the total cost time for SP_3 and SP_7.

Table 1

Optical properties of organs of the MOBY mouse phantom at 700 nm.

	μ_a (mm^{-1})	μ_s (mm^{-1})	g	*n*
Heart	0.038	9.05	0.9	1.33
Liver	0.23	6.48	0.9	1.33
Lung	0.13	21.24	0.9	1.33
Stomach	0.0077	13.77	0.9	1.33
Pancreas	0.043	21.09	0.9	1.33
Kidney	0.043	21.09	0.9	1.33
Spleen	0.23	6.48	0.9	1.33
Intestine	0.0078	10.88	0.9	1.33
Bone	0.039	23.40	0.9	1.33
Brain	0.0027	11.80	0.9	1.33
Bladder	0.0027	11.80	0.9	1.33
Muscle	0.0027	11.80	0.9	1.33